Looking at High-Pressure Electrides Through the Lens of Quantum Crystallography: The Case of Simple Cubic Calcium

Stefano Racioppi,[a] Eva Zurek*[a]

[a] Dr. S. Racioppi, Prof. E. Zurek
Department of Chemistry
State University of New York at Buffalo
777 Natural Science Complex, Buffalo, NY, United States
E-mail: sraciopp@buffalo.edu
E-mail: ezurek@buffalo.edu

Abstract

High-pressure electrides (HPEs) represent a unique class of materials characterized by the localization of electrons in non-bonding interstitial regions, distinct from typical atom-atom interactions. This study delves into the properties of calcium in its simple cubic (sc) phase (Ca-sc) under extreme pressure, a candidate for exhibiting HPE behavior. Through quantum crystallography (QCr), we meticulously analyze the electron density and bonding nature of Ca-sc at pressures up to 40 GPa. Our theoretical framework reveals a pressure-induced electronic transition from s- to d-character, resulting in the formation of multi-center bonds (MCBs) within Ca_8 clusters. The topological analysis corroborates the existence of non-nuclear maxima (NNM) and electron localization features indicative of HPEs. These findings underscore the efficacy of QCr techniques in elucidating material behavior under extreme conditions, thereby establishing a pathway for experimental validation of HPEs like Ca-sc.

Introduction

Understanding the behavior of matter under extreme compression remains a grand challenge in physics, planetary and materials science. It was long assumed that increasing pressure causes all matter to become metallic, comprising ionic cores arranged in close-packed lattices and free electrons (Lai *et al.*, 1991). However, experimental results have shown that this view might be incomplete. Sodium, which at ambient pressure is a metal, becomes transparent to visible light when compressed above a pressure of ~120 GPa (Ma *et al.*, 2009). The transparency is indicative of the opening of a band-gap, meaning the valence electrons are no longer able to move freely in the conduction bands (Ashcroft & Mermin, 1976). Indeed, the calculated band-gap for this new phase of sodium, named Na-hP4, is ~1.3 eV; therefore, sodium becomes a semiconductor under extreme compression (Ma *et al.*, 2009). In fact, sodium becomes a high-pressure electride (HPE), as consequence of the reordering of the valence orbitals, which form 3(s)pd hybrid orbitals, whose overlap results in the formation of a multicentered bond and concomitant localization of electron density in interstitial sites (Racioppi, Storm *et al.*, 2023). A more simplistic model has viewed the electrons as being transferred from the Na atom to so-called interstitial quasi atoms (ISQ) (Miao & Hoffmann, 2014). Though conceptually appealing, this model is not fully supported by detailed analysis of the electronic structure(Racioppi & Zurek, 2024).

The observation of the HPE state of Na-hP4 at pressures above 100 GPa challenges the classic Thomas-Fermi-Dirac (TFD) model, hinting that the physics and chemistry of the elements at extreme conditions has yet to be fully understood (Jeanloz, 2009; Miao *et al.*, 2020; Yoo, 2020). However, sodium is not a high-pressure black swan. For instance, among the complex phase transitions of cesium under pressure, the formation of Cs-IV (Takemura *et al.*, 1982) is accompanied by the reorganization and localization of the electron density in interstitial channels, suggesting the formation of a Cs-electride phase (Von Schnering & Nesper, 1987). Also Cs-IV is characterized by an unusual bonding mechanism triggered by the hybridization of the 6s and 5d valence orbitals (Zurek *et al.*, 2005). Na_2He, having a fluorite-type structure, was predicted to be thermodynamically stable before being synthesized in a Diamond Anvil Cell (DAC) at $P > 113$ GPa and $T > 1500$ K(Dong *et al.*, 2017). Calculations have revealed that the valence electrons of sodium in Na_2He localize in interstitial pockets, making it, theoretically, another possible HPE. In recent years, other materials have been synthesized and proposed as being possible HPEs, including Ca in its simple cubic (sc) form at ~40 GPa (Gu *et al.*, 2009) and Mg-sc, which was observed in ramp compression at 1.32 TPa (Gorman *et al.*, 2022).

All these systems exhibit intriguing open structures, and calculations find that within them electron density is localized in interstitial regions. Nonetheless, a direct experimental proof of this electron localization remains elusive for high-pressure systems. In fact, the HPE state has only been inferred from first-principles calculations, particularly based on Density Functional Theory (DFT), but, so far, never confirmed experimentally. In fact, preparing and characterizing such materials is inherently challenging, whether this is done with static compression in a DAC or with dynamic compression methods.

Crystallography, and particularly X-ray diffraction (XRD), has played a pivotal role in studying exotic HP phases, by linking diffraction patterns and crystal structures with theoretical predictions (Hilleke & Zurek, 2023). However, the full potential of crystallographic experiments to extract chemical and physical information has rarely been exploited in this field. This is where Quantum Crystallography (QCr) offers a promising solution for understanding the nature of HPEs (Grabowsky *et al.*, 2017; Matta, 2018; Genoni *et al.*, 2018; Genoni & Macchi, 2020; Krawczuk & Genoni, 2024).

At the core of Quantum Crystallography is the measurement and calculation of charge density, a key quantum mechanical observable (Genoni *et al.*, 2018). By integrating quantum computations with diffraction data, QCr approaches enable precise determination, and physical interpretation, of the electron density. Modeling the *aspherical* electron distribution collected from single-crystal XRD experiments (Coppens, 1997) through multipolar modeling techniques (Macchi, 2013), such as those based on the Hansen-Coppens formulation (Hansen & Coppens, 1978), is now possible also at high-pressure conditions thanks to the technological advancements in synchrotron and laser facilities (Pascarelli *et al.*, 2023). This modeling can offer deeper insights into the chemical interactions in crystalline materials. Bader's topological analysis, also known as the Quantum Theory of Atoms in Molecules (QTAIM) (Bader, 1990), d-orbital population analysis (Holladay *et al.*, 1983), and investigation of electrostatic potentials(Fournier *et al.*, 2009) and non-covalent interactions(Popelier, 2005), are some of the possible analyses that can be performed on an experimental electron densities. Furthermore, some of these QCr techniques also provide the possibility to constrain/restrain theoretical wave-functions with the experimental electron density (Jayatilaka, 1998). Therefore, by bridging the gap between theory and experiment(Macchi, 2013; Grabowsky *et al.*, 2017; Genoni *et al.*, 2018) QCr could provide a new promising pathway for the experimental observation of HPEs, and by consequence, for a better understanding of their elusive nature.

The usage of QCr techniques has already proven its utility to understand the electronic properties and bonding attitudes in other HP materials(Krawczuk & Genoni, 2024). In the case of syn-1,6:8-13-biscarbonyl[14]annulene(Casati *et al.*, 2016, 2017), the analysis of the electron and current densities, combining experimental and computational methods, has shown that the compound's aromaticity could be partially suppressed by applying an external compression (~ 8 GPa). Further, the elusive behavior of metallophilic interactions as a function of pressure has been investigated in two isostructural copper and silver coordination polymers through XRD and theoretical topological analysis, showing that $Ag^+—Ag^+$ bonds could be triggered by compression, but not $Cu^+—Cu^+$, shedding some light also on the role of relativistic effects in these weak interactions (Racioppi *et al.*, 2020). On other occasions, QCr was used to understand the pressure dependence of the magnetic interactions in metal-organic systems, combining accurate X-ray and neutron diffraction measurements with quantitative modeling of the electron density using spin-polarized DFT (Wehinger *et al.*, 2018). Similarly, Scatena and coworkers(Scatena *et al.*, 2020, 2021), have investigated the orbital reordering, magnetic changes and Jahn-Teller distortion switches in Cu^{2+}-based coordination polymers and perovskites as a function of pressure using in-situ HP X-ray diffraction. Also, the symmetrization of polyiodides in CsI_3 under compression(Poręba *et al.*, 2022) was elucidated thanks to the synergistic cooperation of X-ray diffraction measurements with quantum chemical computations.

It is important to notice that all the aforementioned QCr works at HP were performed in the pressure regime < 20 GPa. Moving towards higher pressures, instead, Na_2He is among the first examples where a newly discovered HPE has been studied using some of the tools of QCr(Dong *et al.*, 2017). Synthesized at P > 113 GPa in a DAC after being computationally predicted, Na_2He is both a neutral helium-based compound and a possible HPE, which was confirmed by the topological analysis of the theoretical electron density. In fact, non-nuclear maxima (NNM) were located at the center of the interstitial sites of Na_2He, where the charge concentration was attributed to the formation of an 8-center two-electron (8c-2e) multi-center bond (MCB) between the surrounding eight sodium atoms. Similarly, the electride nature of Na-hP4(Ma *et al.*, 2009) was elucidated using analogous quantum chemical topology methods(Racioppi, Storm *et al.*, 2023). It was shown that the valence orbitals of Na undergo (s)pd-hybridization and that these new orbitals could constructively combine with these same orbitals from the other sodium atoms comprising the Na_{11} cages, characteristic of the Na-hP4 phase, to form a chemical bond.

To be noted, diffraction is not the only experimental alternative that can leverage theoretical data. For example, it is possible to measure the average electronegativity of a system by probing the ionization energies of all occupied energy levels using various techniques like ultraviolet and X-ray photoelectron spectroscopies (UPS and XPS) (Rahm & Hoffmann, 2015, 2016). This can be combined with purely computational results to evaluate the electronegativity of single atoms in a molecule or in a crystalline material (Racioppi & Rahm, 2021; Racioppi *et al.*, 2024).

In this work we present and highlight the potential benefits that QCr and other quantum-experimental techniques could bring for the study of HPEs. We will do so by focusing on the case of Ca-sc, or Ca-III(Olijnyk & Holzapfel, 1984). This cubic phase of calcium has been observed forming at pressures greater than 35 – 40 GPa(Olijnyk & Holzapfel, 1984; Anzellini *et al.*, 2018) from Ca-bcc (Ca-II) over a wide range of temperatures, from 300 K to 800 K (it is possible that Ca-sc exists also at higher temperatures, since the melting point of Ca at 40 GPa is ~2000 K). It was soon hypothesized that Ca undergoes a pressure induced s- to d-electronic transition(Sutton & Banyard, 1981; Ahuja *et al.*, 1995; Maksimov *et al.*, 2005). In fact, it was predicted that the strongly hybridized s- and d-orbitals of Ca form a MCB inside the cubic Ca_8 cavity,

which corresponds to the generation of the electride state in this system (Novoselov *et al.*, 2020). The MCB mechanism was also proposed by Gu *et al.* in a previous work based on theoretical topological analyses(Gu *et al.*, 2009). However, as any other HPE, the electride state is, so far, only inferred theoretically.

In this work, we will not show experimental evidence for the existence of the electride state in Ca-sc or in any other system. However, we will argue whether it may be possible to provide experimental evidence to support the existence of the HPE state, and discuss if we can learn more about its quantum mechanical nature by combining theory and experiments, in line with the QCr philosophy.

Theoretical Survey

Thermodynamics and Phase Transitions

Before we dive into the Quantum Crystallographic investigation of this system, let's begin with a general survey of the phase transitions that lead to Ca-sc (Ca-III) and familiarize ourselves with the thermodynamics of calcium phases as a function of pressure (Figure 1). Upon compression, Ca follows the fcc → bcc → sc phase transitions. Between 300 – 750 K, the first phase transition from fcc to bcc is observed at ~ 20 GPa, while the second one, from bcc to sc, at ~35 – 40 GPa (Anzellini *et al.*, 2018). Our calculated enthalpies ($H = E + PV$), obtained at 0 K using the meta-GGA exchange-correlation R^{2}SCAN functional (Furness *et al.*, 2020), and in the static lattice approximation (See Computational Details for further information), predict that bcc becomes thermodynamically the most stable phase at 10 GPa, while sc is preferred at 26 GPa (Figure 1). These stability boundaries are systematically lower in pressure compared to the experimental ones. However, zero-point energy corrections and finite temperature effects can easily shift the pressure at which a phase emerges as being the most stable in calculations, and kinetic barriers may inhibit its appearance in experiments. To this point, bcc is observed already at 5 – 10 GPa for T of ~ 800 K (Anzellini *et al.*, 2018). Therefore, we can consider our calculations in quite good agreement with the experimental observations. To be noted, a tetragonal phase having space group *I41/amd*, and an orthorhombic phase, with space group *Cmmm* (identified as a distorted Ca-sc), were also observed at low temperatures between 35 – 40 GPa(Li *et al.*, 2012; Oganov *et al.*, 2010), but we will not discuss these phases in our analyses.
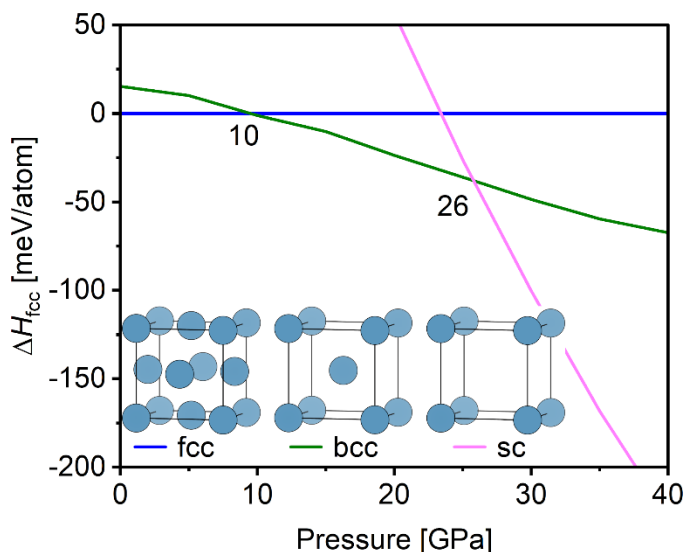
Figure 1. Enthalpy differences ($\Delta H = \Delta E + P\Delta V$) as a function of pressure, for Ca-fcc (Ca-I), Ca-bcc (Ca-II) and Ca-sc (Ca-III), relative to Ca-fcc, calculated with VASP using the meta-GGA exchange-correlation functional R^2SCAN. The optimized lattice parameters for Ca-fcc (0 GPa), Ca-bcc (20 GPa) and Ca-sc (40 GPa) are 5.575 Å, 3.700 Å and 2.38 Å respectively.

The Electronegativity of Ca in Crystalline Phases

All past calculations conclude that Ca-sc will undergo a 4s → 3d electronic transition(Sutton & Banyard, 1981; Ahuja *et al.*, 1995; Maksimov *et al.*, 2005), which is also responsible for the possible transition to the HPE state and the MCB mechanism(Novoselov *et al.*, 2020; Racioppi & Zurek, 2024). Therefore, before investigating in detail the electron density of Ca-sc and solidifying the connection to QCr, it might be useful to have another look at the electronic properties of calcium, and perhaps, to monitor the electronegativity changes as a function of pressure(Rahm, Cammi *et al.*, 2019).

In fact, as we mentioned in the introduction, it is possible to determine the experimental average electronegativity of a system, as defined by Rahm (Rahm, Zeng *et al.*, 2019; Rahm, Cammi *et al.*, 2019; Racioppi, Lolur *et al.*, 2023), by probing the energy of the occupied valence states using spectroscopy techniques such as UPS and XPS(Rahm & Hoffmann, 2015, 2016). Moreover, it is also possible to determine the *in-situ* electronegativity of an atom A inside a material, $\bar{\chi}_A^{val}$, which accounts for all the perturbations introduced by chemical bonding and the crystal field to the more classic electronegativity of an isolated element (Racioppi & Rahm, 2021; Racioppi *et al.*, 2024). In this work, we will present only theoretical values. The procedure for the calculation of $\bar{\chi}_A^{val}$ is reported both in the Computational Details section and in the reference(Racioppi *et al.*, 2024). However, this is our first analysis that connects, in principle, the theoretical realm with experiment observations. We are aware that calcium is generally considered an electropositive element, with a reactivity that usually does not go beyond oxidation with the transfer of two valence electrons. However, exploring the trend of its electronegativity may help us to better understand calcium's reactivity and electronic structure upon compression. In fact, electronegativity does not change at the same rate for all the elements (Rahm, Cammi *et al.*, 2019), meaning that redox reactions can follow different routes under pressure.

In Figure 2 we report various *in-situ* electronegativities of calcium, $\bar{\chi}_{Ca}^{val}$, as: 1) isolated atom, both in gas-phase (which in our nomenclature corresponding to $\bar{\chi}_{Ca}^{0}$, see Computation Details) and under pressure (these values are tabulated in (Rahm, Zeng *et al.*, 2019; Rahm, Cammi *et al.*, 2019)) and 2) atom in a crystalline material for the fcc, bcc and sc (Ca-I, -II and -III respectively) phases in the pressure range from 0 to 40 GPa.
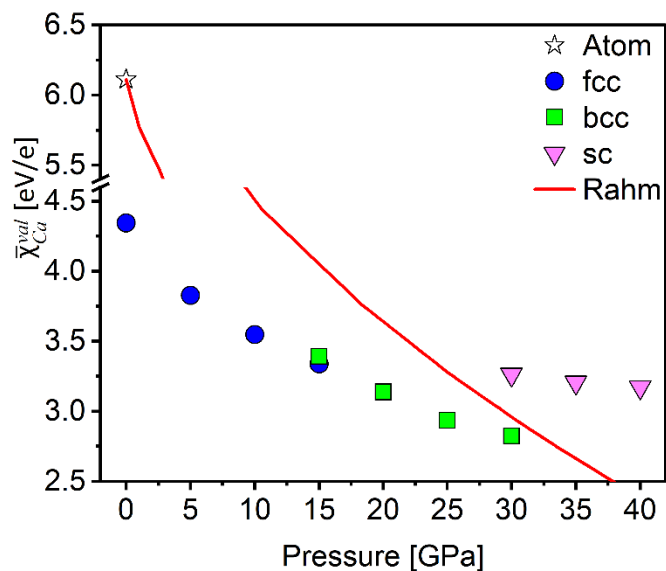
Figure 2. *In-situ* electronegativities, in [eV/e], of calcium, $\bar{\chi}_{Ca}^{val}$. The electronegativity of an isolated atom of calcium $\bar{\chi}_{Ca}^{0}$ (Rahm, Zeng *et al.*, 2019), is labelled as "Atom", while the electronegativity of an isolated atom under pressure (Rahm, Cammi *et al.*, 2019) is marked by the red line. Our calculated *In-situ* electronegativities in the fcc, bcc and sc crystalline phases for calcium, up to 40 GPa, are reported as blue-circles, green-squares and pink-triangles respectively.

At 0 GPa, we readily notice the difference in electronegativity passing from an isolated atom of Ca (calculated to be 6.11 eV/e(Miyabe *et al.*, 2006)), and of Ca in a fcc lattice. The lower value of $\bar{\chi}_{Ca}^{val}$ in the crystalline material is mainly due to the electron-electron interactions, which become the main stabilizing term (See (Rahm & Hoffmann, 2016; Racioppi & Rahm, 2021; Racioppi *et al.*, 2024) for further details on this energy decomposition). Therefore, moving from gas-phase to crystalline material we predict a lowering of the electronegativity of Ca.

The trend of the fcc and bcc electronegativities as a function of pressure is quite in line with the predictions made by Rahm *et al.* (Rahm, Cammi *et al.*, 2019), particularly between 15 and 30 GPa, where the largest difference is of ~0.5 eV/e. However, upon the bcc to sc transition, something changes: the electronegativity of Ca increases with a discontinuity (Figure 2). According to the $\bar{\chi}$ definition of electronegativity(Rahm, Zeng *et al.*, 2019) and its relation with the average orbital energy(Racioppi, Lolur *et al.*, 2023), the increase upon the phase transition to the sc phase is due to the stabilization of some type of orbital. In other words, the valence orbital of calcium experiences either a drastic change in chemical bonding and/or a change in the electronic configuration, which lowers the orbital energy. The known 4s→3d electronic transition that calcium undergoes under pressure(Sutton & Banyard, 1981), is particularly evident from the projected density of states (pDOSs) of Ca-sc, as well as from the spd-hybridized Wannier-function representing the electride's MCB orbital (Figure 3). Could this electronic transition be the driving force for the electronegativity increase?

In the original calculation of the pressure-dependent isolated-atom electronegativities for Ca (red line in Figure 2) the $4s^2 \rightarrow 3d^2$ electronic transition is taken into account. However, in gas-phase, this transition was predicted at $P \geq 60$ GPa (Rahm, Cammi *et al.*, 2019), and accompanied by a spin-state transition from S = 0 (singlet) to S = 1 (triplet), which causes a further lowering of the electronegativity. In Ca-sc there is

no unpaired electron or magnetic moment. Therefore, a similar 4s→3d electronic transition (Ca-sc still retains some 4sp-character even if 3d is the main component(Maksimov *et al.*, 2005), see also Figure 3) has the opposite effect on the electronegativity whether we look at an isolated atom or at an atom in a crystal. Therefore, the increased electronegativity in Ca-sc (*c.f.* green square and pink triangle at 30 GPa in Figure 2) must be caused by an orbital stabilization due to chemical bonding, which is likely the spd-hybrid MCB predicted in past works, and reproduced by us (Figure 3), that is responsible for the creation of the electride state at HP(Novoselov *et al.*, 2020; Racioppi & Zurek, 2024).

This prediction might have some significant consequences in the definition and detection of HPEs: if the sharp increase of the atomic electronegativity of an element, due to the formation of a MCB, is a signature of the transition towards an electride state, it might be possible to experimentally characterize a HPE by probing the binding energies of the valence states of the element before and after the transition. This is a hypothesis that we will explore in future studies. Moreover, this orbital hybridization would also have some interesting implications on the redox reactivity of Ca at HP, since Ca, in its sc phase, becomes more electronegative then zirconium, yttrium or titanium at the same pressure (Rahm, Cammi *et al.*, 2019; Rahm, Zeng *et al.*, 2019)(considering the HP values of the isolated atoms for Zr, Y and Ti), suggesting a possible electronegativity inversion of Ca with these elements at high-pressures.

Now that we have investigated the electronic structure of Ca-sc, and explored the behavior of meaningful chemical properties like the electronegativity, we are ready to look at the bonding features in compressed Ca through the lens of QCr.
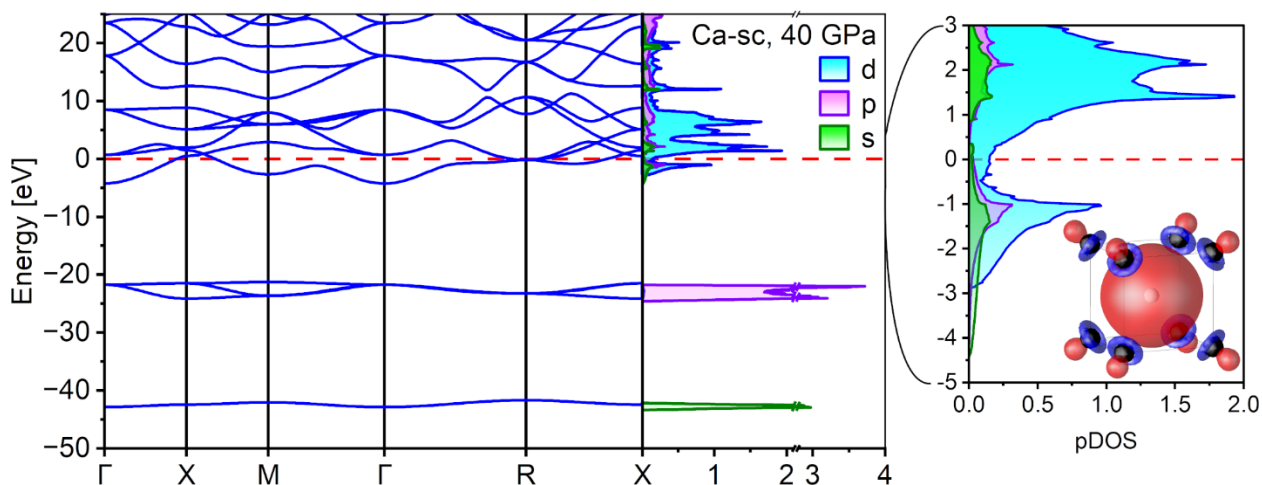
Figure 3. Electronic band structure and projected density of states (pDOSs) of the valence electrons, calculated for Ca-sc at 40 GPa with VASP using the R^{2}SCAN exchange-correlation functional. The inset in the right side of the panel shows the Wannier-function representing the (fifth) valence band of Ca-sc calculated at 40 GPa, which runs around -5 eV below the Fermi level ε_f to ε_f, and corresponding to the electride MCB orbital.

Topological Analysis and Chemical Bonding

The electron density of a chemical system, ρ(**r**), is a quantum mechanical observable that can be either probed with X-ray diffraction experiments or calculated with *ab-initio* methods (Macchi, 2013). This scalar

function gathers quantitative information on chemical bonding and atomic properties, which can be extracted with the QTAIM (Bader, 1990). Even though chemical bonding has no quantum mechanical definition, retrieving chemical properties from an experimental (fully relativistic and fully correlated) electron density (Macchi, 2017), not approximated by levels of theory, can become very useful to verify theoretical models and elucidate the physical nature of crystalline materials.

Therefore, we first want to give a short overview on the importance of topological analyses for the recognition of electrides, which is discussed in more details in prior reviews (Racioppi & Zurek, 2024). To date, there is not a general consensus for a unique definition of HPEs, and many theories have been developed to classify and predict this class of materials in recent years (Miao & Hoffmann, 2014; Racioppi & Zurek, 2024). Nonetheless, it is established that electrides must possess some specific topological features (Postils *et al.*, 2015; Racioppi & Zurek, 2024): 1) the presence of a non-nuclear maximum (NNM) in $\rho(\mathbf{r})$; 2) a largely negative Laplacian of the electron density, $\nabla^2\rho(\mathbf{r})$, at the NNM critical point; and 3) it must be possible to associate a NNM to an ELF basin having a value as close as possible to 1. Ca-sc satisfies all the topological requirements to be classified as an HPE.

However, in absence of high-quality diffraction data, performing an analogous topological survey on the theoretical electron density can still be helpful to rationalize chemical behavior, and perhaps, to guide future experiments. Therefore, we present here (Figure 4a-c) the topological analysis of the electron density of Ca-sc as a function of pressure (from 15 to 40 GPa), together with its electron localization function (ELF). The study of these two quantities ($\rho(\mathbf{r})$ and ELF) is becoming the gold standard to characterize possible HPEs (Postils *et al.*, 2015; Racioppi & Zurek, 2024; Racioppi *et al.*).
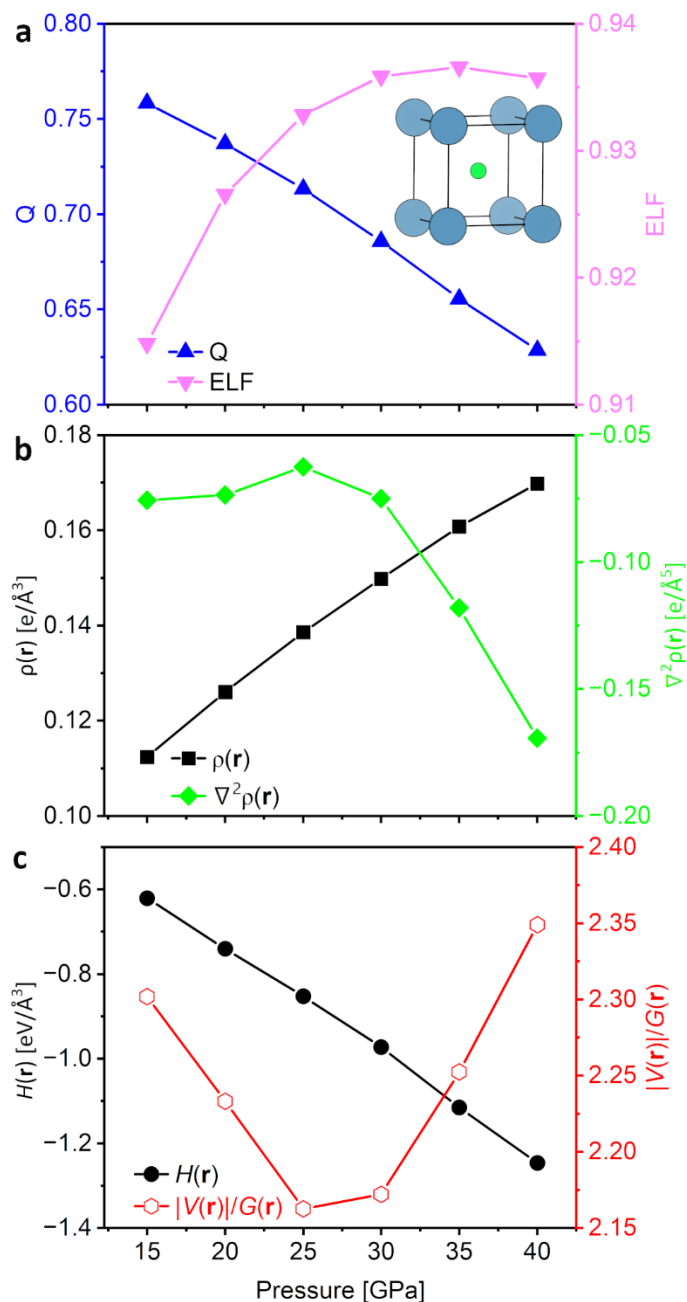
Figure 4. Values at the NNM of **a**) the integrated charge, Q, in Bader's basin, and the electron localization function, ELF; **b**) $\rho(\mathbf{r})$ and $\nabla^2\rho(\mathbf{r})$ (gradient and Laplacian of the electron density) at the NNM; and **c**) local total energy, $H(\mathbf{r})$, and ratio between the modulus of the local potential energy and the local kinetic energy $|V(\mathbf{r})|/G(\mathbf{r})$. The structure of Ca-sc is shown as an inset in (**a**), with the NNM critical point (in green) at the center of the Ca_8 cube.

Before proceeding with our analysis, we must clarify that pure Ca-sc is not observed at *P* < 35 GPa(Anzellini *et al.*, 2018), and that computationally, we predict this phase to become thermodynamically preferred over bcc and fcc only above 26 GPa (Figure 1). However, the computational exploration of a wider range

of pressure for this phase, especially for longer Ca-Ca distances, might give useful insights to understand the type of interactions triggering the electride state.

In Figure 4a, we report the trends, as a function of pressure, of Bader's charge (Q) integrated in the NNM-basin lying at the center of the Ca_8 cubic cluster, together with the value of the ELF at the NNM critical point. Firstly, we notice that the charge Q decreases with compression, despite the increase in the ELF up to a plateau of ~ 0.935. The negative slope of the integrated charge as a function of pressure, already observed in a previous work by Modak and coworkers together with the ELF's plateau (Modak *et al.*, 2023), is opposite to what is calculated for insulating HPEs like Na-hP4 and Na_2He, where the interstitial charges increase upon compression (Dong *et al.*, 2017). Contrary to the sodium-containing systems, Ca-sc is metallic, and as we will clarify later, this is crucial to understanding the inverse charge vs. pressure trend.

Moving to Figure 4b, we can see that the value of $\rho(\mathbf{r})$ at the NNM increases linearly upon compression, meaning that despite the fact that the NNM-basin loses charge (Q, Figure 4a), the value of the electron density at the NNM increases. However, the Laplacian $\nabla^2\rho(\mathbf{r})$, which is related to the level of concentration, or curvature of the electron density at the NNM, has a more interesting behavior. It remains almost constant up to $25 - 30$ GPa, then it steeply decreases, meaning that the level of localization of the electron density at the NNM increases. Interestingly, this variation in the Laplacian happens to correspond with the plateau in the ELF. Therefore, the topology suggests that at $25 - 30$ GPa something changes in the Ca-sc.

Finally, we look at the local energy density at the NNM (Figure 4c). The local total energy density, named $H(\mathbf{r})$, is evaluated at a critical point from the sum of $G(\mathbf{r}) + V(\mathbf{r})$, the local kinetic energy density and the local potential energy density. The local kinetic energy density is calculated according to the Abramov approximation (Abramov, 1997; Espinosa *et al.*, 2001), which positively define $G(\mathbf{r})$ everywhere. On the other hand, the local potential energy is then evaluated according to the local form of the virial theorem, $2G(\mathbf{r}) + V(\mathbf{r}) = 1/4\nabla^2\rho(\mathbf{r})$, which will consequently be negative everywhere in space. In Ca-sc, we calculate that $H(\mathbf{r})$ at the NNM becomes more negative upon compression, with a linear slope, therefore, the Ca_8-MCB becomes stronger. Cremer and Kakra also suggested that negative values of $H(\mathbf{r})$ should be considered as a topological signature for covalent interactions(Cremer & Kraka, 1984). However, this descriptor does not tell us much about the possible change in the chemical interaction, as suggested by the ELF and the Laplacian.

Instead, the ratio defined as $|V(\mathbf{r})|/G(\mathbf{r})$, is more useful to characterize the type of interaction and highlight variations in the local energies (Espinosa *et al.*, 2002; Gatti, 2005; Gervasio *et al.*, 2004). A ratio $|V(\mathbf{r})|/G(\mathbf{r})$ < 1 corresponds to a pure closed-shell interaction region, while $|V(\mathbf{r})|/G(\mathbf{r})$ > 2 is associated to a pure shared-shell interaction region $(1 < |V(\mathbf{r})|/G(\mathbf{r}) < 2$ is the intermediate region)(Gatti, 2005). Therefore, the NNM in Ca-sc corresponding to the center of the Ca_8 interaction is topologically characterized as a shared-shell, since $|V(\mathbf{r})|/G(\mathbf{r})$ > 2, which is in line with ours and previous Wannier-function analyses (Novoselov *et al.*, 2020), and overall, the MCB model. Moreover, $|V(\mathbf{r})|/G(\mathbf{r})$ is calculated to increase above 25 GPa, showing that, despite the fact that the total charge Q in the basin decreases, the overlap between the spd-hybrid orbitals of Ca_8 increases.

On the other hand, $|V(\mathbf{r})|/G(\mathbf{r})$ also increases by decompressing from 25 GPa (therefore, reentering in the stability-pressure regime of bcc). Calculating the projected density of states (pDOS) at variable pressures (15, 25 and 40 GPa, See Figure 5), we can see that upon decompression the d-states become less and less dominant, while the s-state increase both in dispersion and magnitude. Therefore, we could interpret the

results of Figure 4c and Figure 5 as a change in the spd-hybridization, where at lower pressures, the 4s-character, more diffuse than the 3d orbitals, is dominant, since it better overlaps at longer distances; while at higher pressures (shorter distances), the 3d-character becomes the dominant one, and stronger thanks to its higher degree of localization. The decrease of the 4s-dispersion upon compression is probably a consequence of the increased localization of charge density at the center of the cell, since broadened and diffuse bands are more characteristics of metallic states. Moreover, the Pauli repulsion between two neighboring 4s-4s orbitals and the closer contact between 4s-components having different phase might also affect the s-states at higher pressures. A similar effect has also been observed in pressurized Li and Li(NH$_3$)$_4$(Zurek *et al.*, 2011). Since Ca-sc is experimentally observed only at $P > 30 - 35$ GPa, our topological analysis suggests that the stability of this phase of calcium is strictly connected to the overlap-ability of the 3d orbitals. To be noted, if Ca-sc is decompressed below 10 GPa, the NNA and the electride state disappear.
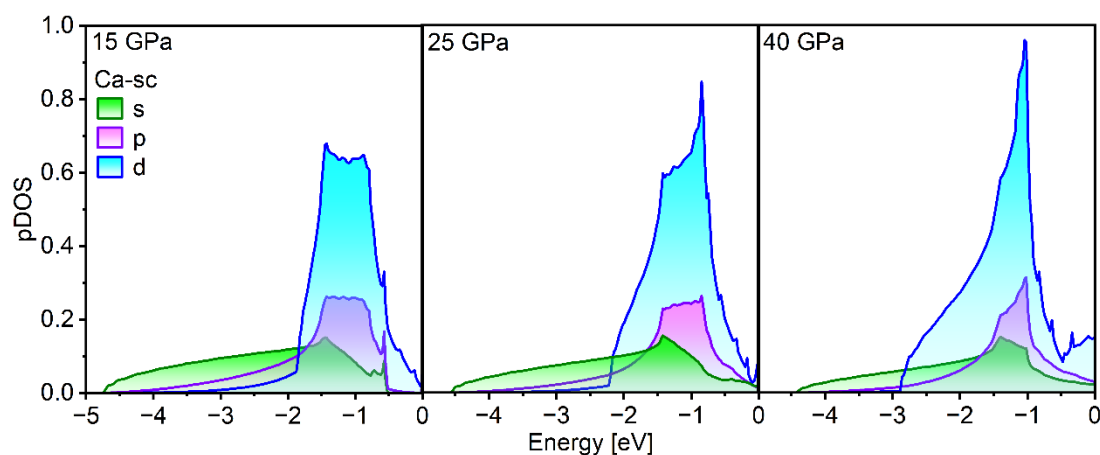

Figure 5. Projected density of states (pDOSs) calculated for Ca-sc at 15, 25 and 40 GPa with VASP using the R^{2}SCAN exchange-correlation functional. The optimized lattice parameters of Ca-sc at 15, 25 and 40 GPa are 2.917 Å, 2.778 Å and 2.38 Å respectively.

The Inverted Charge vs. Pressure Trend

The final aspect we would like to elucidate is the negative trend of Q upon compression (Figure 4a). We have mentioned earlier that this is related with the metallic character of Ca-sc, but now we will look at it in more detail. In Figure 6, we show the top two bands (the fifth and the sixth bands, considering that we are explicitly treating 10 valence electrons in calcium, and that there is only one atom per unit cell) that cross the Fermi level in Ca-sc at different pressures, respectively, drawn as solid and dashed-lines. Moreover, we show the charge density rendered at some important high symmetry points of the reciprocal space. At low pressure (20 GPa), mostly the bottom band (solid line) is occupied, while the upper dashed-band corresponds almost completely to a conduction band, but no band-gap is created. Then, upon compression, the energy levels of the bands shift. At the *X* point, the bottom solid-band goes up in energy becoming partially unoccupied (hole pocket), corresponding to a Lifshitz transition (a change in the topology of the Fermi surface (Wu *et al.*, 2023)). This corresponds to a partial removal of charge density

from the center of the Ca_8 cluster (Figure 6). At the same time, the top dashed-band becomes partially occupied at R (electron pocket), which results in an accumulation of charge density at the faces of the Ca cube. The faces of the cube are also the regions where the pure 3dxy, 3dxz and 3dyz orbitals overlap(Novoselov *et al.*, 2020). Therefore, the trend of decreasing Q with respect to pressure trend shown in Figure 4a is a direct consequence of the metallic nature of Ca-sc, and caused by the population/depopulation of two bands crossing the Fermi level at two different symmetry points (Lifshitz transition), which delocalize the charge density from the center of the Ca_8-cube to the faces.

Interestingly, Dunn and Bundy measured the resistivity of Ca under pressure finding it to increase above 0.4 ohm at 4.2 K and 30 GPa, before dropping to 0.2 ohm at 44 GPa at the same temperature, and vanishing below 2 K, possibly due to a superconducting state transition(Dunn & Bundy, 1981). Therefore, the inverted integrated-charge trend (Figure 4) might also be correlated with the electrical conductivity of Ca-sc.
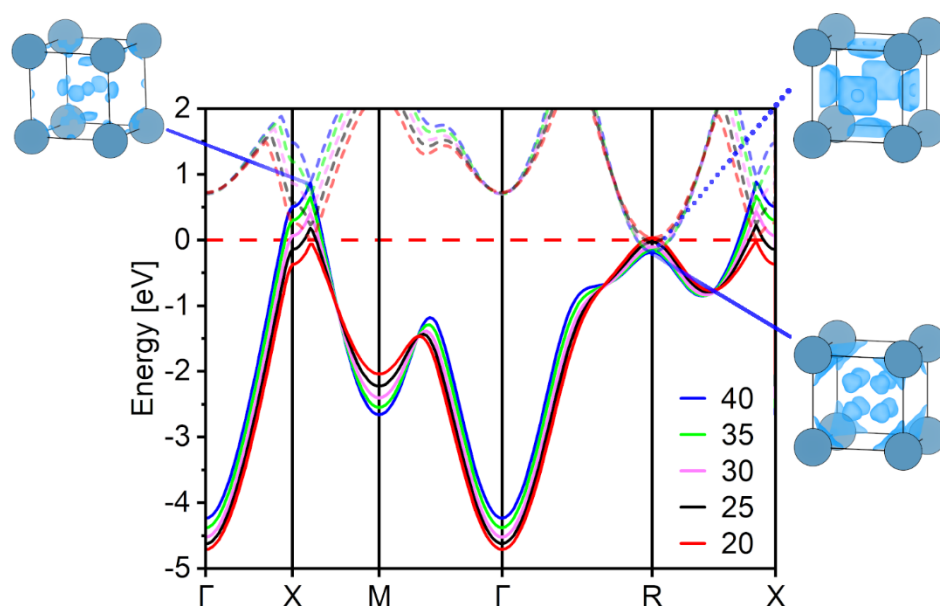
Figure 6. Plot of the fifth (solid line) and sixth (dashed line) electronic bands of Ca-sc (1 atom per unit cell and 10 explicit electrons) as a function of pressure, from 20 to 40 GPa. The insets represent the rendered partial charge densities (specifically taken from the calculation at 40 GPa) at different high symmetry points in the reciprocal space.

Conclusions

Using calcium's simple cubic (sc) phase, this study emphasizes the potential role of quantum crystallography (QCr) in enhancing our understanding of high-pressure electrides (HPEs). The electronegativity of an atom, or the topology of the crystalline electron density, are features that can be calculated using quantum mechanical methods as well as measured and quantified experimentally. By modelling the electronic structure of calcium under pressure with the r^2SCAN functional, we have performed a series of theoretical experiments to show the numerous chemical and physical information that can be unlocked by QCr. Utilizing advanced topological analyses of the electron density, we obtained results that support the HPE nature of Ca-sc and it's formation through the multi-center bonding (MCB)

model via the hybridization of spd-orbitals, which has been proposed in past works (Gu *et al.*, 2009; Novoselov *et al.*, 2020). Our results also confirm that the emergence of the HPE state is closely tied to the emergence of orbital hybridization and stabilization of the d-states under pressure. Moreover, we have performed the very first theoretical survey of the electronegativity evolution of an element upon several high-pressure phase transitions in the solid state, which can be probed experimentally using spectroscopic techniques. This survey highlighted an unexpected jump in the electronegativity of calcium upon transition to the sc-phase, which could become an additional signature for detecting the formation of the electride state. The application of QCr methodologies in this computational study serves as a bridging framework between theoretical predictions with the potential experimental validation for understanding the electronic structure and bonding attitudes of HPEs. These findings lay a solid foundation for future experimental endeavors aimed at characterizing and confirming these elusive high-pressure phases, ultimately enriching our understanding of complex materials under extreme conditions.

Acknowledgements

Computational Details

We performed periodic Density Functional Theory (DFT) calculations using the Vienna *Ab-Initio* Simulation Package (VASP, version 6.2.1)(Kresse & Hafner, 1993) and the BAND package, version 2022.101, developed by Software Chemistry & Materials (SCM)(Philipsen *et al.*).

For VASP, the R^{2}SCAN exchange-correlation functional was employed(Furness *et al.*, 2020) for the geometry optimizations and calculations of the electronic properties. The projected augmented wave (PAW) method(Blöchl, 1994) was used treating explicitly 10 valence electrons, with a cutoff of 1000 eV. The *k*-point mesh was generated using the Γ-centered Monkhorst-Pack scheme(Monkhorst & Pack, 1976), and the number of divisions along each reciprocal lattice vector was selected so that the product of this number with the real lattice constant was greater than or equal to 60 Å. For the geometry optimizations, the accuracy of the energy convergence was set to 10^{-6} eV and the norms of all the forces calculated during the relaxations were smaller than 10^{-3} (eV/Å). The tetrahedron smearing method was adopted in the calculations of the electronic properties(Blöchl *et al.*, 1994). The topological analysis of the electron density, based on the Quantum Theory of Atoms in Molecules (QTAIM),(Bader, 1990) was performed using the Critic2(Otero-De-La-Roza *et al.*, 2014) code.

For BAND, the crystal structures optimized with VASP were used in the calculation of the electronic properties and to evaluate the atomic electronegativities. The R^{2}SCAN exchange-correlation functional was employed(Furness *et al.*, 2020). All the Ca electrons were included in our calculations (equal to 20 electrons), and no frozen core was imposed. Scalar relativistic effects were also included using the Zero Order Regular Approximation (ZORA) (Philipsen *et al.*, 1997). A double-ζ polarized (DZP) basis set was used for Ca to permit the convergence of the self-consistent field (SCF) for the high-pressure structures(Kadantsev *et al.*, 2007). The integration quality was kept equal to 'Very Good' for all calculations.

For the calculation of the atomic electronegativity, we adopted the procedure reported in (Racioppi *et al.*, 2024). The electron energy density, X, was evaluated as

$$X \approx \sum_i n_i \varepsilon_i = \int_{-\infty}^{\varepsilon_f} \varepsilon \cdot DOS(\varepsilon) d\varepsilon$$

where n_i is the number of electrons having energy ε_i, and i runs over all the occupied states. This corresponds to the integral, up to the Fermi level ε_f, of all the density of states (DOSs) multiplied by the energy of the states. In the case of Ca-sc, there is only one atom in the unit cell, therefore, the total electron energy density X also corresponds to the atomic electron energy density X_A. Then, the average atomic electron energy $\bar{\chi}_A$ is calculated dividing X_A by the total number of electrons explicitly treated for the atom A, n_A, which equals to 20 for Ca.

The *in-situ* electronegativity of an element in a material, denoted as $\bar{\chi}_A^{val}$, is then calculated as follows:

$$\bar{\chi}_A^{val} = \bar{\chi}_A^0 + \Delta\bar{\chi}_A$$

where $\bar{\chi}_A^0$ is the isolated atom's reference value of electronegativity, which in this work, is take from (Rahm, Zeng *et al.*, 2019), while $\Delta\bar{\chi}_A$ is calculated as

$$\Delta\bar{\chi}_A = \bar{\chi}_A - \bar{\chi}_{A,vac}$$

and $\bar{\chi}_{A,vac}$ is the average atomic electron energy calculated for the isolated atom in vacuum. $\Delta\bar{\chi}_A$ essentially rescales the standard electronegativity of the isolated atom.

Therefore, in the case of Ca-sc, $\bar{\chi}_{Ca}$ is the average electron energy of Ca in the sc structure; $\bar{\chi}_{Ca,vac}$ is the average atomic electron energy calculated for an isolated atom of Ca and $\bar{\chi}_{Ca}^0$ is the electronegativity value of Ca as tabulated by (Rahm, Zeng *et al.*, 2019), and equal to 6.1 eV/e (Miyabe *et al.*, 2006). To be noted, $\Delta\bar{\chi}_{Ca}$ is calculated accounting for all the electrons of Ca, while $\bar{\chi}_{Ca}^0$ (6.1) refers to the electronegativity of the valence electrons only. Therefore, it is assumed that $\Delta\bar{\chi}_{Ca}$ accounts principally for the variation of the valence electron energy, as explained in (Racioppi *et al.*, 2024).

TB-LMTO calculations,(Andersen & Jepsen, 1984) using the Cs-sc structural parameters at 40 GPa, were performed using the Vosko Wilk Nusair, exchange-correlation potential, plus Perdew-Wang non-local exchange-correlation (Vosko *et al.*, 1980; Perdew & Wang, 1992). Scalar relativistic effects were included. The basis set consisted of spd LMTOs on the Ca atoms and sp LMTOs on the empty spheres (positions of the ISQs to account for the Ca basis-set polarization). The calculations utilized a 25x25x25 mesh in the tetrahedron *k*-space integrations. The version of the *N*MTO program employed(Zurek *et al.*, 2005) is not self-consistent and requires the output of the self-consistent potential from the TB-LMTO program. The occupied bands obtained with the full *N*MTO basis set yielded bands that were in good agreement with those calculated with VASP-R^{2}SCAN with the 10 valence electrons POTCAR.

The downfolded *N*MTO band structures were then compared with the bands computed employing the full *N*MTO basis set. The band structure computed by only placing an s-orbital on every empty sphere (ISQ) and choosing an energy mesh that spanned the valence band was able to describe the valence band well, except at the R-point where this band is triply degenerate. In this calculation, all of the partial waves on the Ca atoms were downfolded and the s-like partial waves on the empty spheres were used in the basis. The resulting WF is plotted in the manuscript, and it could be described as forming from a constructive overlap of spd-hybrid orbitals of the 8 Ca atoms that surround the empty sphere. This Wannier-function differs from the one calculated by Novoselov *et al.*(Novoselov *et al.*, 2020) as it spans only one band, whereas previously a basis that also included the 5d orbitals on the Ca atoms was constructed.

References

Abramov, Y. A. (1997). *Acta Crystallogr. Sect. A Found. Crystallogr.* **53**, 264–272.

Ahuja, R., Eriksson, O., Wills, J. M. & Johansson, B. (1995). *Phys. Rev. Lett.* **75**, 3473–3476.

Andersen, O. K. & Jepsen, O. (1984). *Phys. Rev. Lett.* **53**, 2571–2574.

Anzellini, S., Errandonea, D., Macleod, S. G., Botella, P., Daisenberger, D., De'Ath, J. M., Gonzalez-Platas, J., Ibáñez, J., McMahon, M. I., Munro, K. A., Popescu, C., Ruiz-Fuertes, J. & Wilson, C. W. (2018). *Phys. Rev. Mater.* **2**, 083608.

Ashcroft, N. W. & Mermin, N. D. (1976). Vol. *Solid State Physics*, edited by D. G. Crane. p. 395. New York: Saunders College Publishing.

Bader, R. F. W. (1990). Atoms in molecules: a quantum theory, International series of monographs on chemistry Oxford: Oxford Science Publications.

Blöchl, P. E. (1994). *Phys. Rev. B - Condens. Matter Mater. Phys.* **50**, 17953–17979.

Blöchl, P. E., Jepsen, O. & Andersen, O. K. (1994). *Phys. Rev. B* **49**, 16223–16233.

Casati, N., Genoni, A., Meyer, B., Krawczuk, A. & Macchi, P. (2017). *Acta Crystallogr. Sect. B Struct. Sci. Cryst. Eng. Mater.* **73**, 584–597.

Casati, N., Kleppe, A., Jephcoat, A. P. & Macchi, P. (2016). *Nat. Commun.* **7**, 10901.

Coppens, P. (1997). X-Ray Charge Densities and Chemical Bonding New York: Oxford University Press.

Cremer, D. & Kraka, E. (1984). *Croat. Chem. Acta* **57**, 1259–1281.

Dong, X., Oganov, A. R., Goncharov, A. F., Stavrou, E., Lobanov, S., Saleh, G., Qian, G. R., Zhu, Q., Gatti, C., Deringer, V. L., Dronskowski, R., Zhou, X. F., Prakapenka, V. B., Konôpková, Z., Popov, I. A., Boldyrev, A. I. & Wang, H. T. (2017). *Nat. Chem.* **9**, 440–445.

Dunn, K. J. & Bundy, F. P. (1981). *Phys. Rev. B* **24**, 1643–1650.

Espinosa, E., Alkorta, I., Elguero, J. & Molins, E. (2002). *J. Chem. Phys.* **117**, 5529–5542.

Espinosa, E., Alkorta, I., Rozas, I., Elguero, J. & Molins, E. (2001). *Chem. Phys. Lett.* **336**, 457–461.

Fournier, B., Bendeif, E. E., Guillot, B., Podjarny, A., Lecomte, C. & Jelsch, C. (2009). *J. Am. Chem. Soc.* **131**, 10929–10941.

Furness, J. W., Kaplan, A. D., Ning, J., Perdew, J. P. & Sun, J. (2020). *J. Phys. Chem. Lett.* **11**, 8208–8215.

Gatti, C. (2005). *Zeitschrift Fur Krist.* **220**, 399–457.

Genoni, A., Bučinský, L., Claiser, N., Contreras-García, J., Dittrich, B., Dominiak, P. M., Espinosa, E., Gatti, C., Giannozzi, P., Gillet, J. M., Jayatilaka, D., Macchi, P., Madsen, A., Massa, L., Matta, C. F., Merz, K. M., Nakashima, P. N. H., Ott, H., Ryde, U., Schwarz, K., Sierka, M. & Grabowsky, S. (2018). *Chem. - A Eur. J.* **24**, 10881–10905.

Genoni, A. & Macchi, P. (2020). *Crystals* **10**, 473.

Gervasio, G., Bianchi, R. & Marabello, D. (2004). *Chem. Phys. Lett.* **387**, 481–484.

Gorman, M. G., Elatresh, S., Lazicki, A., Cormier, M. M. E., Bonev, S. A., McGonegle, D., Briggs, R., Coleman, A. L., Rothman, S. D., Peacock, L., Bernier, J. V., Coppari, F., Braun, D. G., Rygg, J. R., Fratanduono, D. E., Hoffmann, R., Collins, G. W., Wark, J. S., Smith, R. F., Eggert, J. H. & McMahon, M. I. (2022). *Nat. Phys.* **18**, 1307–1311.

Grabowsky, S., Genoni, A. & Bürgi, H. B. (2017). *Chem. Sci.* **8**, 4159–4176.

Gu, Q. F., Krauss, G., Grin, Y. & Steurer, W. (2009). *Phys. Rev. B - Condens. Matter Mater. Phys.* **79**, 134121.

Hansen, N. K. & Coppens, P. (1978). *Acta Crystallogr. Sect. A* **34**, 909–921.

Hilleke, K. P. & Zurek, E. (2023). Vol. *Comprehensive Inorganic Chemistry III*, edited by K. Poeppelmeier & J. Reedijk. Elsevier.

Holladay, A., Leung, P. & Coppens, P. (1983). *Acta Crystallogr. Sect. A* **39**, 377–387.

Jayatilaka, D. (1998). *Phys. Rev. Lett.* **80**, 798–801.

Jeanloz, R. (2009). *Phys. World* **22**, 34–37.

Kadantsev, E. S., Klooster, R., De Boeij, P. L. & Ziegler, T. (2007). *Mol. Phys.* **105**, 2583–2596.

Krawczuk, A. & Genoni, A. (2024). *Acta Crystallogr. Sect. B Struct. Sci. Cryst. Eng. Mater.* **80**, 249–274.

Kresse, G. & Hafner, J. (1993). *Phys. Rev. B* **47**, 558–561.

Lai, D., Abrahams, M. & Shapiro, S. (1991). *Astrophys. J.* **377**, 612–628.

Li, B., Ding, Y., Yang, W., Wang, L., Zou, B., Shu, J., Sinogeikin, S., Park, C., Zou, G. & Mao, H. K. (2012). *Proc. Natl. Acad. Sci. U. S. A.* **109**, 16459–16462.

Ma, Y., Eremets, M., Oganov, A. R., Xie, Y., Trojan, I., Medvedev, S., Lyakhov, A. O., Valle, M. & Prakapenka, V. (2009). *Nature* **458**, 182–185.

Macchi, P. (2013). *Crystallogr. Rev.* **19**, 58–101.

Macchi, P. (2017). *Acta Crystallogr. Sect. B Struct. Sci. Cryst. Eng. Mater.* **73**, 330–336.

Maksimov, E. G., Magnitskaya, M. V & Fortov, V. E. (2005). *Physics-Uspekhi* **48**, 761–780.

Matta, C. F. (2018). *J. Comput. Chem.* **39**, 1019–1020.

Miao, M. S. & Hoffmann, R. (2014). *Acc. Chem. Res.* **47**, 1311–1317.

Miao, M., Sun, Y., Zurek, E. & Lin, H. (2020). *Nat. Rev. Chem.* **4**, 508–527.

Miyabe, M., Geppert, C., Kato, M., Oba, M., Wakaida, I., Watanabe, K. & Wendt, K. D. A. (2006). *J. Phys. Soc. Japan* **75**, 034302.

Modak, P., Verma, A. K. & Oppeneer, P. M. (2023). *Phys. Rev. B* **107**, 125152.

Monkhorst, H. J. & Pack, J. D. (1976). *Phys. Rev. B - Condens. Matter Mater. Phys.* **13**, 5188–5192.

Novoselov, D. Y., Korotin, D. M., Shorikov, A. O., Oganov, A. R. & Anisimov, V. I. (2020). *J. Phys. Condens. Matter* **32**, 445501.

Oganov, A. R., Ma, Y., Xu, Y., Errea, I., Bergara, A. & Lyakhov, A. O. (2010). *Proc. Natl. Acad. Sci. U. S. A.* **107**, 7646–7651.

Olijnyk, H. & Holzapfel, W. B. (1984). *Phys. Lett.* **100A**, 191–194.

Otero-De-La-Roza, A., Johnson, E. R. & Luaña, V. (2014). *Comput. Phys. Commun.* **185**, 1007–1018.

Pascarelli, S., McMahon, M., Pépin, C., Mathon, O., Smith, R. F., Mao, W. L., Liermann, H. P. & Loubeyre, P. (2023). *Nat. Rev. Methods Prim.* **3**, 82.

Perdew, J. P. & Wang, Y. (1992). *Phys. Rev. B* **45**, 13244–13249.

Philipsen, P. H. T., Velde, G. te, Baerends, E. J., Berger, J. A., Boeij, P. L. de, Franchini, M., Groeneveld, J. A., Kadantsev, E. S., Klooster, R., Kootstra, F., M.C.W.M. Pols, P. R., Raupach, M., Skachkov, D. G., Snijders, J. G., Verzijl, C. J. O., Gil, J. A. C., Thijssen, J. M., Wiesenekker, G., Peeples, C. A., Schreckenbach, G. & Ziegler, T. *BAND 2022.1, SCM, Theor. Chem. Vrije Univ. Amsterdam, Netherlands, Http//Www.Scm.Com*.

Philipsen, P., van Lenthe, E., Snijders, J. & Baerends, E. (1997). *Phys. Rev. B - Condens. Matter Mater. Phys.* **56**, 13556–13562.

Popelier, P. L. A. (2005). *Struct. Bond.* **115**, 1–56.

Poręba, T., Racioppi, S., Garbarino, G., Morgenroth, W. & Mezouar, M. (2022). *Inorg. Chem.* **61**, 10977–10985.

Postils, V., Garcia-Borràs, M., Solà, M., Luis, J. M. & Matito, E. (2015). *Chem. Commun.* **51**, 4865–4868.

Racioppi, S., Andrzejewski, M., Colombo, V., Sironi, A. & Macchi, P. (2020). *Inorg. Chem.* **59**, 2223–2227.

Racioppi, S., Hyldgaard, P. & Rahm, M. (2024). *J. Phys. Chem. C* **128**, 4009–4017.

Racioppi, S., Lolur, P., Hyldgaard, P. & Rahm, M. (2023). *J. Chem. Theory Comput.* **19**, 799–807.

Racioppi, S. & Rahm, M. (2021). *Chem. – A Eur. J.* **27**, 18156–18167.

Racioppi, S., Saffarian-Deemyad, I., Holle, W., Belli, F., Ferry, R., Kenney-Benson, C., Smith, J. S., Zurek, E. & Deemyad, S. *ArXiv:2312.17498 [Cond-Mat.Supr-Con]*.

Racioppi, S., Storm, C. V., McMahon, M. I. & Zurek, E. (2023). *Angew. Chem. Int. Ed.* **27**, e202310802.

Racioppi, S. & Zurek, E. (2024). *ChemRxiv*.

Rahm, M., Cammi, R., Ashcroft, N. W. & Hoffmann, R. (2019). *J. Am. Chem. Soc.* **141**, 10253–10271.

Rahm, M. & Hoffmann, R. (2015). *J. Am. Chem. Soc.* **137**, 10282–10291.

Rahm, M. & Hoffmann, R. (2016). *J. Am. Chem. Soc.* **138**, 3731–3744.

Rahm, M., Zeng, T. & Hoffmann, R. (2019). *J. Am. Chem. Soc.* **141**, 342–351.

Scatena, R., Andrzejewski, M., Johnson, R. D. & Macchi, P. (2021). *J. Mater. Chem. C* **9**, 8051–8056.

Scatena, R., Montisci, F., Lanza, A., Casati, N. P. M. & Macchi, P. (2020). *Inorg. Chem.* **59**, 10091–10098.

Von Schnering, G. H. & Nesper, R. (1987). *Angew. Chem.* **26**, 1059–1080.

Sutton, A. & Banyard, K. E. (1981). *J. Phys. F Met. Phys.* **11**, 805.

Takemura, K., Minomura, S. & Shimomura, O. (1982). *Phys. Rev. Lett.* **49**, 1772–1775.

Vosko, S. H., Wilk, L. & Nusair, M. (1980). *Can. J. Phys.* **58**, 1200–1211.

Wehinger, B., Fiolka, C., Lanza, A., Scatena, R., Kubus, M., Grockowiak, A., Coniglio, W. A., Graf, D., Skoulatos, M., Chen, J. H., Gukelberger, J., Casati, N., Zaharko, O., Macchi, P., Krämer, K. W., Tozer, S., Mudry, C., Normand, B. & Rüegg, C. (2018). *Phys. Rev. Lett.* **121**, 117201.

Wu, L., Chi, S., Zuo, H., Xu, G., Zhao, L., Luo, Y. & Zhu, Z. (2023). *Npj Quantum Mater.* **8**, 4.

Yoo, C. S. (2020). *Matter Radiat. Extrem.* **5**, 018202.

Zurek, E., Jepsen, O. & Andersen, O. K. (2005). *ChemPhysChem* **6**, 1934–1942.

Zurek, E., Wen, X. D. & Hoffmann, R. (2011). *J. Am. Chem. Soc.* **133**, 3535–3547.